Digest Journal of Nanomaterials and Biostructures Vol. 19, No. 1, January - March 2024, p. 337 - 350

Fabrication and anti-corrosion performances of robust superhydrophobic surface on NAB via solution-etching

K. Chen, G. D. Fan, Y. M. Xia*, J. F. Ou
School of Materials and Engineering, Jiangsu University of Technology, Changzhou 213001, China

A labyrinth microstructure interconnected by micron and submicron acicular structures was successfully prepared by immersing nickel-aluminum bronze in 9 wt% $FeCl_3 \cdot 6H_2O$ solution at room temperature for 40 min. After being modified with 1H, 1H, 2H, 2H-perfluorodecyltriethoxysilane (FAS-17), the microstructure surface displays robustly low-adhesion superhydrophobicity, and the water contact angle is above 160 ° on it. In addition, the superhydrophobic surface exhibits excellent corrosion resistance and stability in 3.5wt % NaCl aqueous solution and corrosion solution with different pH values.

(Received November 28, 2023; February 28, 2024)

Keywords: Super-hydrophobicity, Corrosion, Stability, Wettability, Thin films

1. Introduction

Nickel-aluminum bronze (NAB) is widely used in machinery manufacturing and marine industries, due to its excellent physical, chemical and mechanical properties [1]. Nevertheless, the poor corrosion resistance in harsh working conditions, such as moist atmosphere and marine environment, leads to a shortened service life and limits the application range of NAB products [2]. Consequently, the preparation of protective surface is an effective anti-corrosion strategy for NAB component products, as well it remains a grand challenge.

Inspired by the famous “lotus effect”, super-hydrophobic surface (SHS) has been developed by different methods, including the sol-gel method [3,4], chemical etching [5], electrodeposition [6] and so on, to enhance the resistant corrosion performances of metals. Furthermore, owing to the advantages of high efficiency, fast preparation, diverse structure and morphology, low requirements for a variety of materials and equipment, chemical etching method to prepare superhydrophobic surface has become one of the most ideal superhydrophobic surface preparation methods. For example, Qian [7]et al. prepared a super-hydrophobic film with enhanced anti-corrosion resistant performance on NAB by picosecond laser. However, up till now, very limited literatures have been reported, which involve the preparation of protective films on NBA surface via solution-etching methods to realize long-term corrosion resistance.

Here, we report the preparation of anti-corrosion SHS with labyrinth microstructure on NAB via solution-etching. The effects of etching time and concentration of etching solution on the wettability of the surface were discussed in detail, and that SHS preparation conditions were

* Corresponding author: xiaweiwei906@126.com
https://doi.org/10.15251/DJNB.2024.191.337

optimized. Additionally, the corrosion resistance performances were evaluated via electrochemical measurement in detail. The relationship between SHS preparation conditions and corrosion resistance was also explored. And these findings are significant to develop innovative SHS for high-effective corrosion resistance performances.

2. Experimental section

2.1. Sample preparation

Superhydrophobic surfaces on NAB were fabricated via two-step process, combining acicular microstructure etching and surface fluorination. Fabrication methods and more details are as follows.

2.1.1. Etching rough microstructure of superhydrophobic surfaces

Typically, NAB sheet substrate samples (size: 13 mm × 13 mm × 3 mm) and electrodes (size: 10 mm × 10 mm × 3 mm) were polished with different grades of emery paper (600 mesh and 1200 mesh), cleaned by sonication in acetone, ethanol, and deionized water for 5 min respectively, and dried using a cold air blower. The NAB sheet and NAB electrode were etched with 60 mL aqueous solution of $FeCl_3 \cdot 6H_2O$ (3 wt% -18 wt%) contained 1 mL HCl (36 wt%) at room temperature for different time, and then the NAB samples and electrodes were washed with ethanol and deionized water and dried again.

2.1.2. Surface fluorination

Surface fluorination of the NAB samples and electrodes was carried out in a vacuum dryer with 2 mL FAS-17 at the bottom beforehand at room temperature for 10 h. and then the fluorinated samples and electrodes were obtained for pending test.

2.2. Experimental details

2.2.1. Materials

Chemicals used include ferric chloride hexahydrate ($FeCl_3 \cdot 6H_2O$, ≥98.0%), ethanol (C_2H_5OH, ≥99.7%), acetone (CH_3COCH_3, 99.5%), hydrochloric acid (HCl, 36%), and 1H, 1H, 2H, 2H-perfluorodecyltriethoxysilane (FAS-17) were obtained from Sinopharm Chemical Reagent Co., Ltd., China. All the chemical reagents were used as received without further purification.

2.2.2. Instruments and Characterization

Scanning electron microscopy (SEM) images were taken by a Sirion field-emission scanning electron microscope (FEI) at 20 kV. X-ray diffraction (XRD) patterns were performed with an X-ray diffractometer model D8-Discover (Bruker) with Cu Kα radiation (λ = 1.5418 Å). The sessile drop method was used for water CA measurements using contact angle machine ((DSA-30, Kruss, Germany) contact-angle system at ambient temperature. Water droplet (5 μL) was dropped carefully onto the surface. The average CA value was determined by measuring 5 times at different spots of the same sample. The RA of water was measured under the same condition and the volume of the droplet was 10 μL.

2.2.3. Electrochemical experiments

The electrochemical measurements were performed at room temperature in a conventional three-electrode electrochemical cell consisted of a NAB / NAB-SHS electrode (exposed area 1

cm^2) as working electrode, a platinum as counter electrode and a saturated calomel electrode (SCE) as the reference electrode by using an electrochemical workstation (Refrence 3000, Gamry Company, USA). 3.5wt.% NaCl aqueous solution was used as simulated seawater electrolyte and corrosion medium. All measured potentials presented in this paper were referred to SCE. The potentiodynamic polarization curves were measured between -0.5V and 0.5V (vs. OCP) with the scanning rate of 1 mV/s. The electrochemical impedance spectroscopy (EIS) measurements were conducted in the frequency range of 100 KHz to 0.05 Hz at open circuit potential with amplitude of 5 mV. Prior to each electrochemical test, the NAB electrodes were immersed in a corrosive medium (3.5wt.% NaCl aqueous solution) for 30 min to obtain a steady electrochemical state.

3. Results and discussion

3.1. Surface structural morphology and wettability behavior analysis

Our previous studies found that at room temperature, etching time and etching concentration are crucial to etched rough structure and static contact angle on NAB substrate surface.

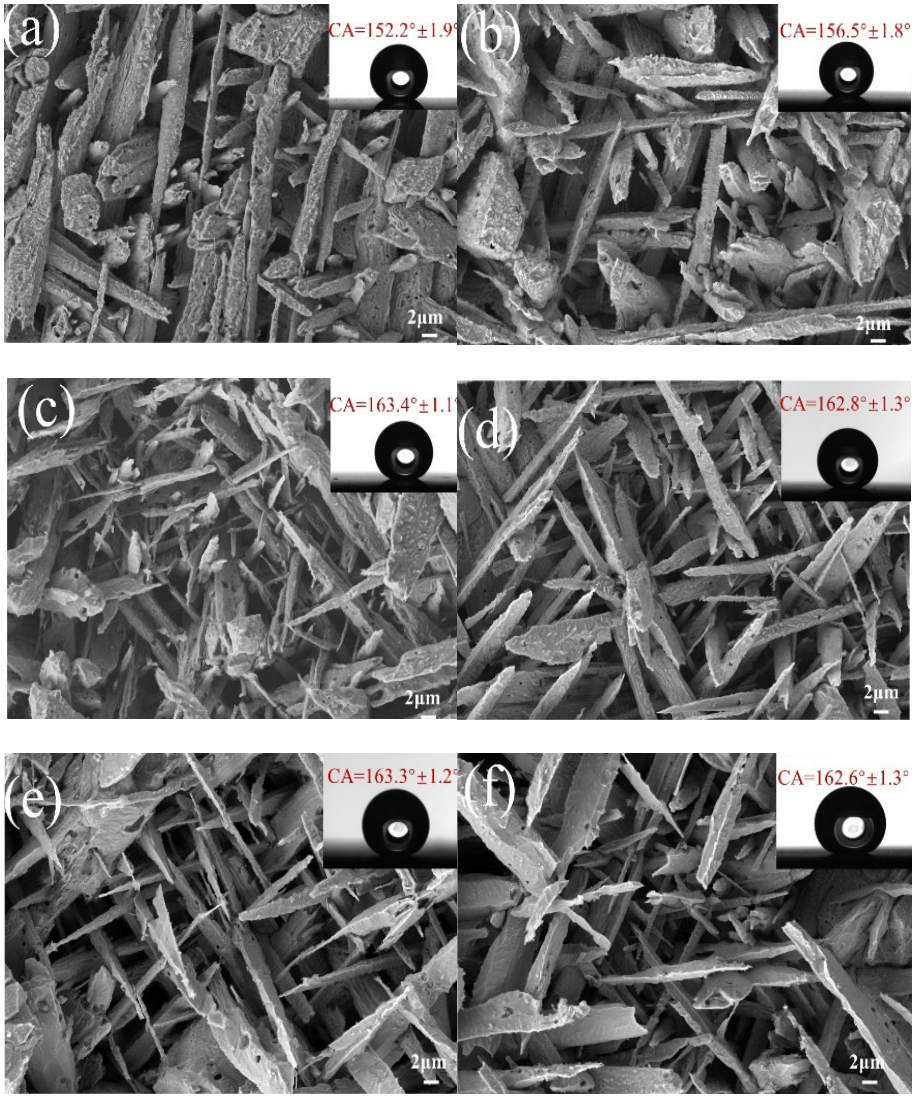

Fig. 1. (a-f) SEM images of as-etched sample surfaces in etching solution of 3 wt%, 6 wt%, 9 wt%, 12 wt%, 15 wt% and 18 wt% $FeCl_3 \cdot 6H_2O$ at room temperature for 40 min,respectively. The insets (top-right) are images of water droplets (5 μL) on the corresponding fluorinated samples, respectively.

Figure 1 shows the SEM images and the corresponding static water contact angle optical images of as-etched NAB sample surfaces in etching solution of 3 wt%, 6 wt%, 9 wt%, 12 wt%, 15 wt% and 18 wt% $FeCl_3 \cdot 6H_2O$ concentration at room temperature for 40 min, respectively. As demonstrated in Figure 1a-1f, in different concentration etching solution, NAB substrates all obtained labyrinth microstructures interconnected by etched acicular and columnar structure, which can all achieve superhydrophobicity after fluorination. As the concentration of the etching solution increases, the static water contact angle on fluorinated as-etched NAB surfaces gradually increases, untill it tends to remain constant (stable state). In lower concentration etching solution, the etched structure is coarse, unevenly distributed and unstable hydrophobic, as shown in Figure 1a and Figure 1b. From Figure 1c, 1d, 1e and 1f, in relatively high concentration etching solution, the etched structure is fine, uniform, stablely hydrophobic. Furthermore, when the etching concentration is not less than 9 wt% , the static water contact angle on the fluorinated as-etched structure is more than 160 °. And the sample surfaces etched in 9 wt% -18 wt% $FeCl_3 \cdot 6H_2O$ solution almost have an equal hydrophobic effect, possessing excellently uniform microstructure and steady and strong superhydrophobicity. In view of wetting behavior and economic effect (cost savings), the optimized concentration of the etching solution is including 9 wt% $FeCl_3 \cdot 6H_2O$.

Figure 2 demonstrates the surface morphology and a static water contact angle optical image of NAB samples before and after etching. Figure 2a is SEM image of the non-treated NAB surface, showing that the bare substrate is relatively smooth with many grinding and polishing lines. As exhibited in Figure 2b, Figure 2c, Figure 2d, Figure 2e and Figure 2f, via etching in 9 wt% $FeCl_3 \cdot 6H_2O$ solution at room temperature for different etching time, the acicular and columnar microstructures are obtained. As can be seen in Figure 2b, micrometre size labyrinth is non-uniformly distributed and formed by the interconnected etched columnar microstructure, and the microcolumns etched for 10 min are typically 5 μm ~ 20 μm in length, 1 μm ~ 6 μm in width and1 μm ~ 5 μm in thickness. Figure 2c and Figure 2d illustrate the microstructures and the dimensions etched for 20 min and 30 min are similar, but the structure is finer and more well-distributed than that etched for 10 min. On the other hand, the submicron scale structures constructed by the acicular rods etched over 30 min are comparatively well-distributed, as shown in Figure 2e and Figure 2f. To sum up, with the prolonging of etching time, the etched structure becomes relatively fine, dense and uniform, and the structure regularity of orientation and distribution obviously increases. At the same time, after fluorination, the corresponding surface hydrophobicity is improved from 85 ° to 151°, 155°, 157°, 163° and 162°, respectively. These facts illustrate the as-etched micron and submicron scale structures, significantly improving the substrate surface roughness, create favorable conditions for the realization of superhydrophobicity. Moreover, the submicron scale structures etched over 30 min has a stronger ability to capture air than the micrometre structures etched below 30 min. Considering wetting behavior and productivity, the optimized etching time is 40 min.

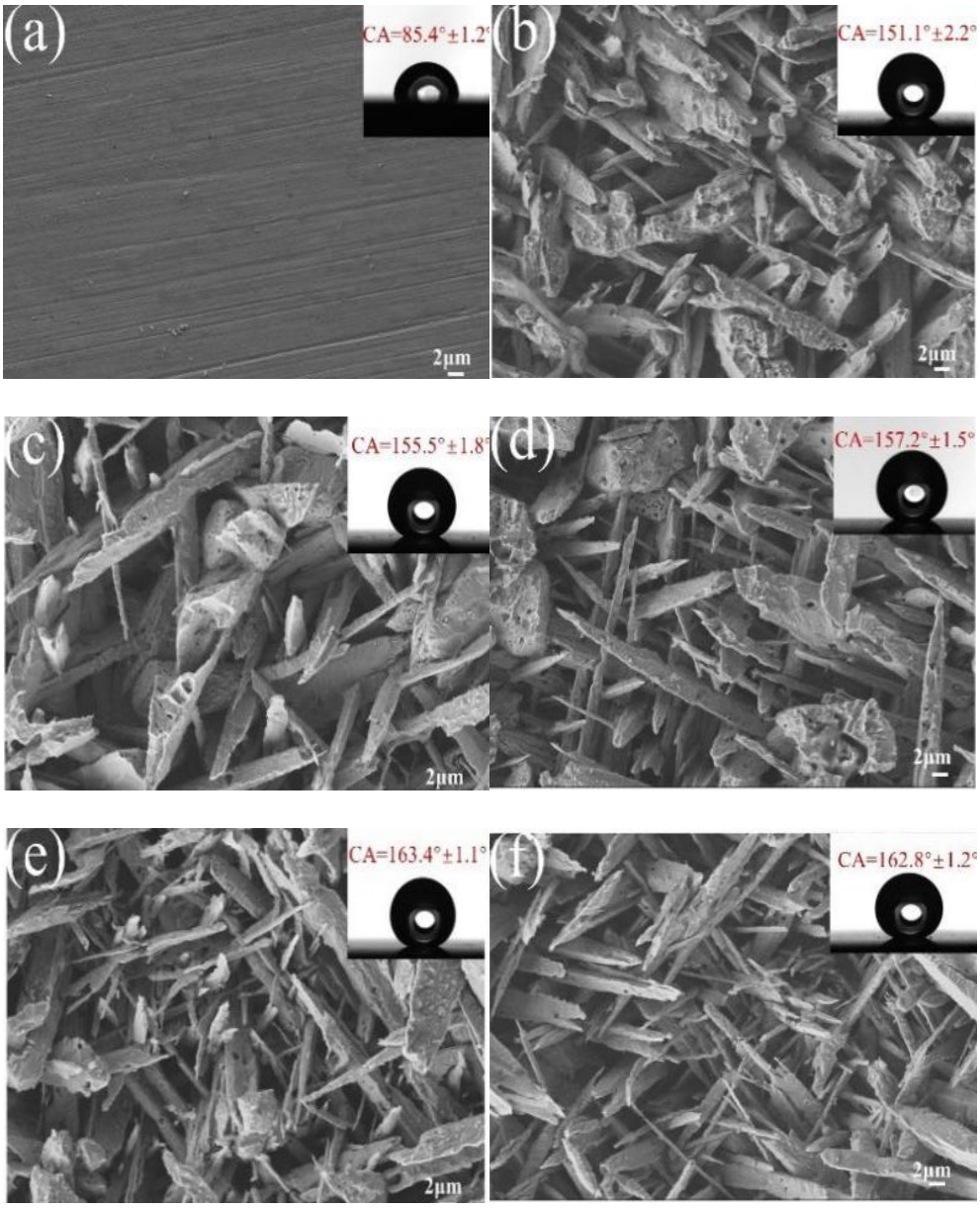

Fig. 2. (a-f) SEM images of sample surfaces: (a) bare NAB surface, (b-f) as-etched products in 9 wt% $FeCl_3 \cdot 6H_2O$ solution at room temperature for 10, 20, 30, 40, and 50 min, respectively. The insets (top-right) are images of water droplets (5 μL) on the corresponding fluorinated samples, respectively.

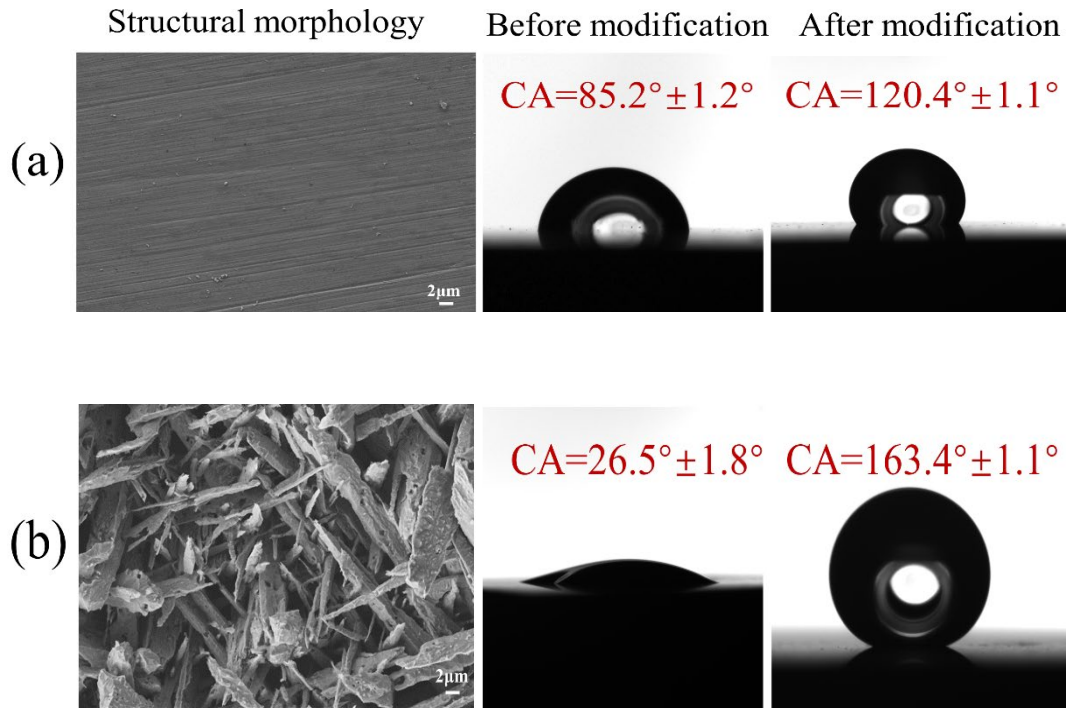

Fig. 3. Comparison images of water droplets (5 μL) on the surfaces of (a) bare NAB sheet and (b) NAB sample etched in 9 wt% $FeCl_3 \cdot 6H_2O$ solution at room temperature for 40 min.

Figure 3a demonstrates the optical images of a water droplet on bare NAB surface before and after modification with FAS-17. The non-treated NAB is hydrophilic with a static water CA of 85.2 °, and the post-fluorination pristine NAB is hydrophobic with a static water CA of 120.4 °. From Figure 3, as etching time increasing to 40 min, the surface roughness steady increased, the hydrophilicity of the surface was enhanced with decreasing static water CA to 26.5 °; after fluorination, the CA of the corresponding surface increased to 163.4 °, and the rolling angle decreasing to 9.3 °. To sum up, NAB sample etched in 9 wt% $FeCl_3 \cdot 6H_2O$ solution at room temperature for 40 min is superhydrophobic with low adhesion. It is well known that the construction of superhydrophobic surfaces requires micro-nano rough structures and low surface energy. The labyrinth microstructure interconnected by etched micron and submicron scale acicular and columnar structures created favorable conditions for the realization of strong superhydrophobicity, which shows that the unique microstructure can contribute to trapping large amount of air and the air cushion would prevent water droplet from penetrating into NAB substrate.

It is worth mentioning that FAS-17 is a substance with extremely low surface energy, and the post-fluorination substrate has extremely low surface energy and excellent hydrophobic properties. Figure 4 displays the schematic process of immobilization of FAS-17 on the NAB surfaces. Self-assembly process of FAS-17 on NAB surface is as follows. Firstly, FAS-17 molecule reacts with water vapor in the air on the NAB surface to convert its siloxane group ($Si\text{-}OC_2H_5$) into silanol groups (Si-OH). Secondly, as an active group, the silanol group undergoes a dehydration condensation reaction with the hydroxyl group (-OH) on the surface of the NAB substrate, which results in a covalently bonded silanes on the NAB surface [8]. Finally, as the

reaction continues, an extremely thin fluorinated layer of NAB surface is gradually formed. Thus, the surface energy of post-fluorination NAB substrate is greatly reduced, and the static water contact angle is sharply increased.

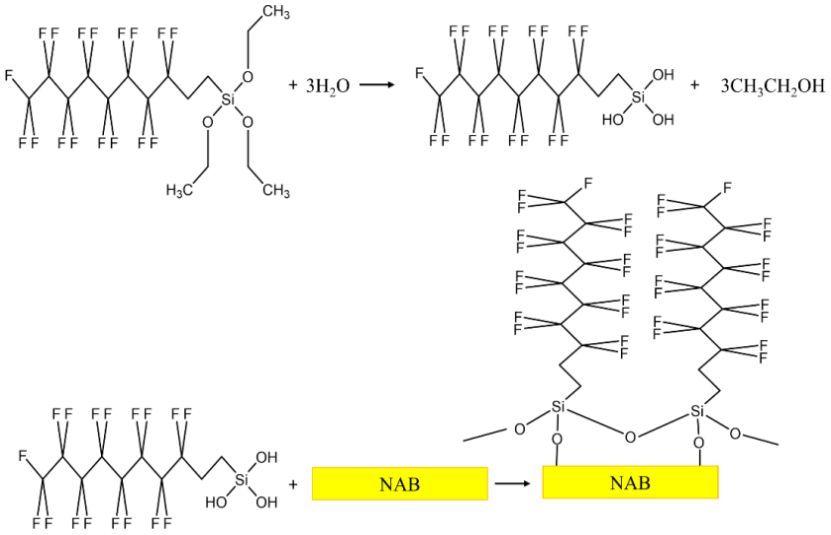

Fig. 4. The reaction process of FAS-17 on the NAB surface of labyrinth microstructure interconnected by etched micron and submicron scale acicular and columnar structures.

3.2. Phase and composition analysis

Figure 5 shows XRD patterns of several typical NAB samples. The XRD pattern of bare NAB substrate demonstrates that the detectable peaks can be readily indexed to face-centered cubic structure elemental copper (JCPDS Card No. 04–0836) with fine crystallinity and intermetallic compound kappa (κ) phase mainly composed of Fe, Al and Ni elements, as indicated in Figure 5 (bare NAB sample). And the composition of NAB phases is in accordance with the EDS result in Figure 6a. This result is consistent with the reported as-cast state NAB material [9–11]. NAB alloy in as-cast state is composed of a columnar crystal structure of copper-rich α solid solution and a small amount of β phase or retained martensitic β' phase. At the same time, there are also various types of κ phase, mainly composed of Fe, Al and Ni elements. Since the α phase and the residual β' phase have similar lattice parameters, there is obvious peak overlap. Being similar to the α phase and the β' phase, the diffraction peak from various types of κ phase is also difficult to be distinguished, so various κ phases are grouped into a single peak corresponding to the (Fe, Ni) Al phase (110) [12–14]. As shown in Figure 5 (modified NAB sample) and Figure 5 (bare NAB sample), the diffraction patterns of NAB substrate before and after modification with FAS-17 remain almost unchanged. It is due to the fact that the fluorination layer is extremely thin and has light weight, being insufficient to cause detectable changes in the diffraction spectrum. The XRD pattern of fluorinated NAB sample etched in 9 wt% $FeCl_3 \cdot 6H_2O$ solution at room temperature for 40 min still displays the same diffraction spectrum of the original substrate, which illustrates that etched microstructure on NAB substrate via $FeCl_3 \cdot 6H_2O$ solution barely have the $FeCl_3$ residual. This result can further be confirmed by the EDS spectrum of etched NAB surface modified by FAS-17 in Figure 6b, which contained F and Si but did not include Cl element.

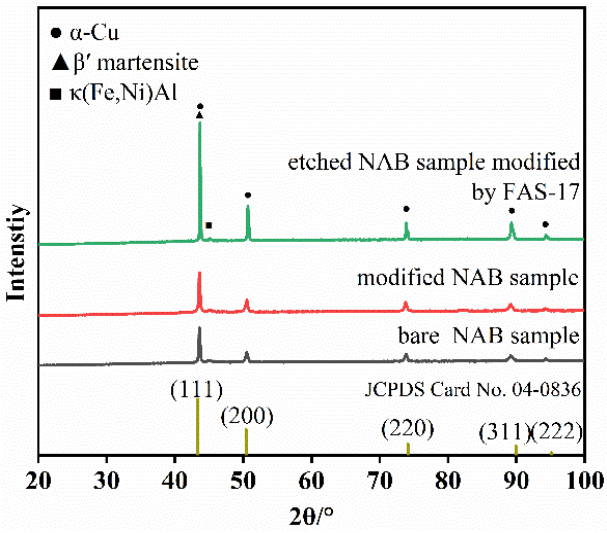

Fig. 5. XRD patterns of bare NAB substrate, modified pristine NAB sample by FAS-17and typical etched NAB sample modified by FAS-17, respectively.

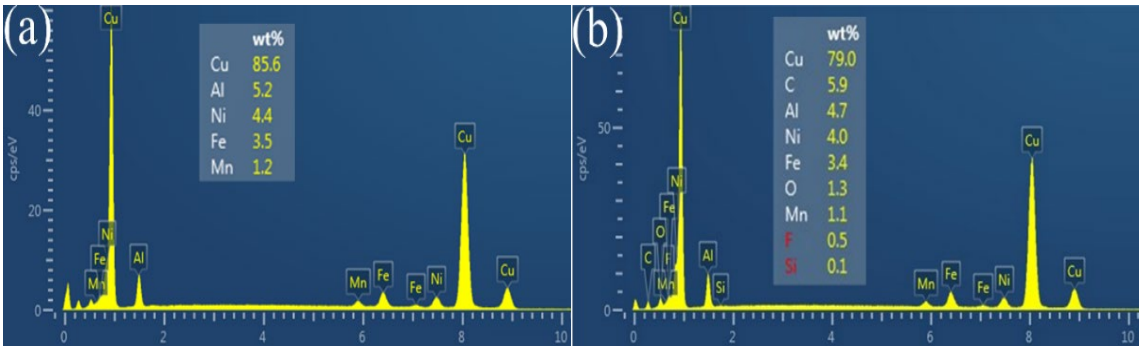

Fig. 6. Energy dispersive spectroscopy (EDS) results of selected areas of bare NAB surface (a) and (b) etched NAB surface modified by FAS-17, respectively.

3.3. Corrosion resistance analysis

The potentiodynamic polarization plots are displayed in Figure 7. The corrosion potential (E_{corr}), corrosion current density (I_{corr}) and inhibition efficiency (η) of all electrodes obtained by extrapolating the linear portions of the potentiodynamic polarization plots to the intersection are summarized in Table 1. The η is calculated by Eq [15,16]. (1):

$$\eta\% = \frac{I_{corr}^{0} - I_{corr}}{I_{corr}^{0}} \times 100\% \tag{1}$$

Generally, a low corrosion current density or a high corrosion potential in the polarization curve indicates a low corrosion rate and good corrosion resistance [17]. It can be seen from Figure

7 that compare with bare NAB electrode, the NAB electrodes modified by FAS-17 obtained higher corrosion potential and lower corrosion current density. Icorr of NAB samples before and after modification decreased from 1.772×10^{-5} A · cm^{-2} to 1.261×10^{-5} A · cm^{-2}, and 1.765×10^{-6} A · cm^{-2}, respectively. Especially, the Icorr of low-adhesion SHS NAB electrode etched in 9 wt% $FeCl_3 \cdot 6H_2O$ solution at room temperature for 40 min was reduced more than one magnitude in contrast to bare NAB electrode. And its inhibition rate reached 90.03%. It is on account of surface properties of low-adhesion SHS electrode. And the NAB SHS has a special microstructure modified by FAS-17 to form a dense protective layer, where water droplets appear Cassie-Baxter state [18]. On the one hand, the labyrinth microstructure interconnected by etched acicular and columnar structures can trap and store a large amount of air, reducing the contact area with the corrosive medium, which leaded to retard further corrosion reactions. On the other hand, surface layer fluorinated by FAS-17 had a low conductivity and impeded chemical reactions in the corrosive medium, thereby reducing the self-corrosion current density.

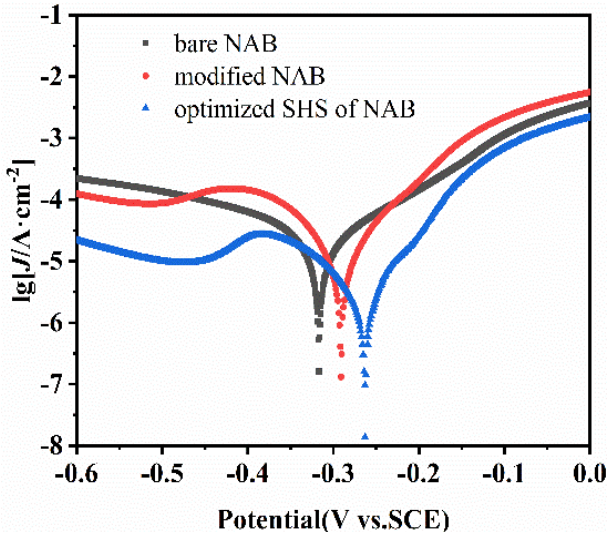

Fig. 7. Potentiodynamic polarization curves of bare NAB, modified NAB and optimized SHS of NAB etched in 9 wt% $FeCl_3 \cdot 6H_2O$ solution at room temperature for 40 min.

Table 1. The E_{corr}, I_{corr} and η of bare NAB electrode, modified NAB electrode and optimized SHS of NAB electrode etched in 9 wt% $FeCl_3 \cdot 6H_2O$ solution at room temperature for 40 min in 3.5 wt% NaCl solution.

Sample	E_{corr}(mV)	I_{corr}(A·cm^{-2})	η(%)
bare NAB	-316	1.772×10^{-5}	/
modified NAB	-295	1.261×10^{-5}	28.83
optimized SHS of NAB	-263	1.765×10^{-6}	90.03

Moreover, corrosion kinetics behavior was studied by electrochemical impedance spectroscopy (EIS). Nyquist curves, composed of capacitance arcs at high frequencies and Waburg impedances at low frequencies, of bare NAB and post-fluorination NAB surfaces with the different structure are depicted in Figure 8. The semicircle in the high frequency region is closely

related to the electric double layer capacitance (Qdl) and charge transfer resistance (Rct). It is well known that superhydrophobic surfaces can be considered as porous media for storing air. When the capacitive arc is concave, the reason why the frequency dispersion was imposed may be the inhomogeneity and roughness of the substrate surface [19,20]. And the presence of low-frequency Warburg impedance indicates that the electrochemical reaction process of NAB in 3.5wt % NaCl is not only controlled by the charge transfer step process but also affected by the diffusion process. It is related to the movement of dissolved oxygen from the solution to the electrode surface or the outward diffusion process of NAB dissolved products from the electrode surface. It is generally known that a bigger diameter of semicircles in Nyquist plot stand for a better corrosion resistance property [21–23].Bare NAB exhibited a small radius in the Nyquist plot at the high frequency part. NAB surface modified by FAS-17 displayed a slightly big diameter of semicircles. However, the SHS possess the radius much larger than that of bare NAB and fluorided NAB, indicating that it would be good anti-corrosion property in the NaCl solution. This can be attributed the fact that the superhydrophobic surface with labyrinth microstructure can greatly reduce the contact area between the electrolyte and the substrate, effectively suppress the transfer of corrosive ions, and sharply improve the corrosion resistance.

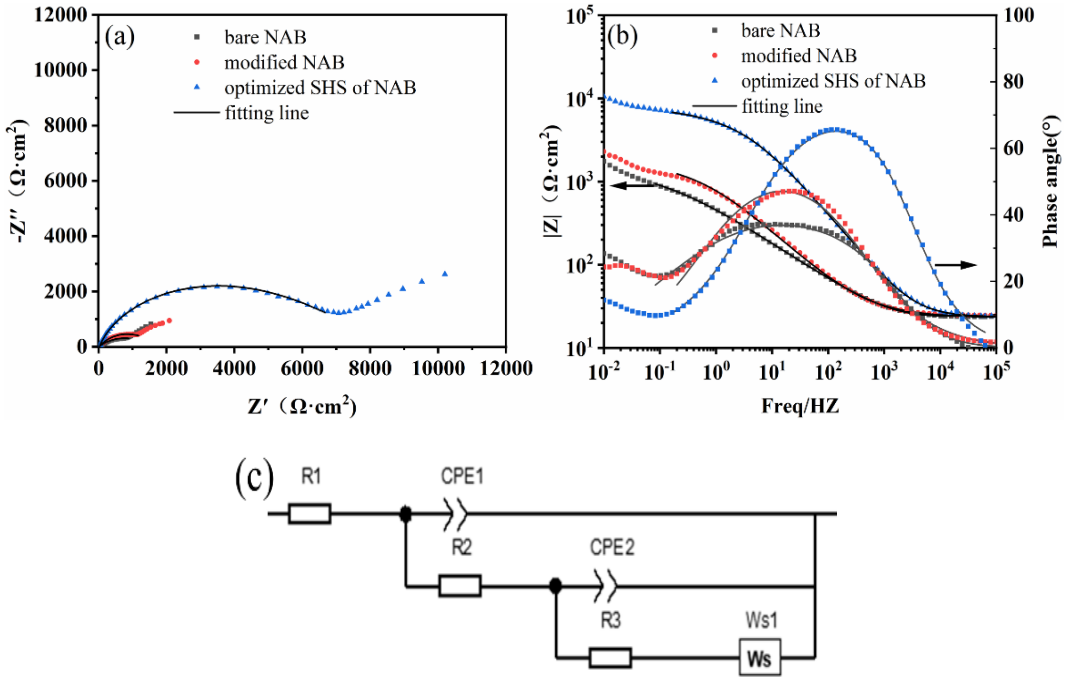

Fig. 8. Nyquist plots (a) and Bode diagrams (b) of bare NAB, modified NAB and optimized SHS of NAB etched in 9 wt% $FeCl_3 \cdot 6H_2O$ solution at room temperature for 40 min, respectively.(c)EIS fitting equivalent circuit diagram of optimized SHS of NAB etched in 9 wt% $FeCl_3 \cdot 6H_2O$ solution at room temperature.

As shown in Figure 8b, bare NAB substrate possessed the lowest impedance modulus |Z| in low frequency range, while superhydrophobic NAB substrate still maintained a high impedance modulus |Z|, suggesting a good anti-corrosion property. The results confirm that SHS performs excellent corrosion resistance to protect the bare NAB surface. In additionally, the above

electrochemical results demonstrate that low-adhesion SHS largely improved the corrosion resistance of the NAB substrates. And the protective capability of the low-adhesion SHS probably originates from both the anti-water property and the physical diffusion barriers of SHS coatings.

3.4. Stability analysis

In practical applications, mechanical stability and chemical stability directly determine the durability of superhydrophobic surfaces. A lot of methods for evaluating the stability of superhydrophobic surfaces were reported, among them, mechanical wear is considered as the most widely used method for evaluating the mechanical durability [24]. The mechanical stability of superhydrophobic NAB surface was tested by using 1000 mesh sandpaper under 100 g load. The specific operations are as follows. The superhydrophobic NAB substrate loaded with 100 g was placed on the yarn paper and then moved slowly in the same direction at a constant speed. Undergoing a 20 cm load friction movement every time, the substrate was retested the corresponding water static contact angle on it. The recorded results are shown in Figure 9a. Withstanding longer move distance, the substrate has a smaller wetting angle. When the moving distance reaches 120 cm, superhydrophobicity of the superhydrophobic NAB substrate is completely lost. Due to continuous wear, the hydrophobic molecular layer and microstructure of the SHS surface are broken, resulting in the decreasing contact angle. In addition, utilizing HCl and KOH to adjust pH values of corrosion solution, the chemical stability of the SHS NAB surface was tested. The superhydrophobic NAB was immersed in corrosion solution with different pH values for 1 h, and then the contact angle was measured and recorded, as illustrated in Figure 9b. Apart from the strong acid condition, the static water CA on SHS NAB is very stable in weak acid, neutral and alkaline solution conditions.Hence,it is believed that the SHS NAB surface generally has good chemical stability.

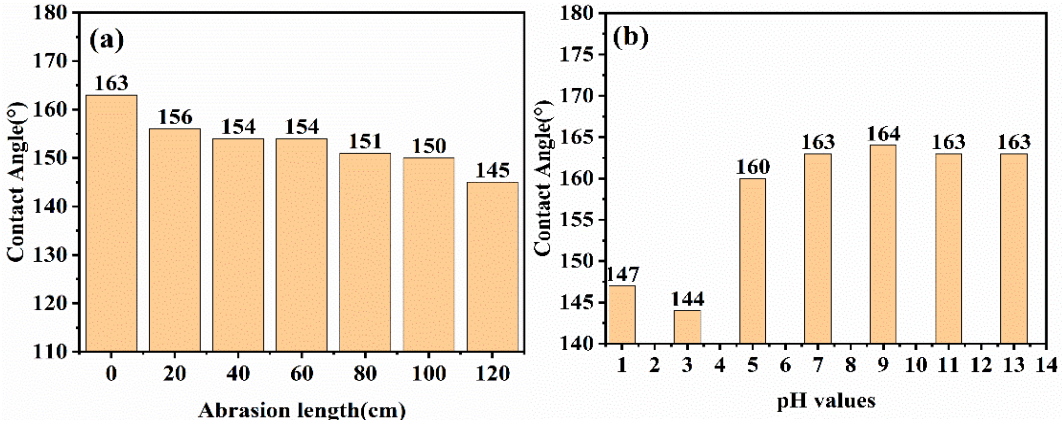

Fig. 9. (a) The change of contact angle of superhydrophobic nickel-aluminum bronze surface with friction distance (b) The change of contact angle of superhydrophobic nickel-aluminum bronze surface with pH values.

3.5. Non-sticking behavior analysis

Except the rolling angle testing, in order to further confirm that the prepared superhydrophobic NAB surface has extremely low adhesion, a method reported by Zhang [25]and

Liu [26] was used. In the experiment, a 5 μL water droplet hanging on the top of injection needle slowly come into contact with the superhydrophobic NAB surface. When the water droplet contacted with superhydrophobic surface, the droplet continue to be squeezed. It was found that the water droplet shifted from the original position and adhered to the outer wall of the needle tube. Then, during the lifting process of the injection needle tube, the water droplet did not adhered to the superhydrophobic surface and was very easily leaved with the needle tube. The findings aboved indicate that the prepared superhydrophobic NAB surface has extremely low adhesion.

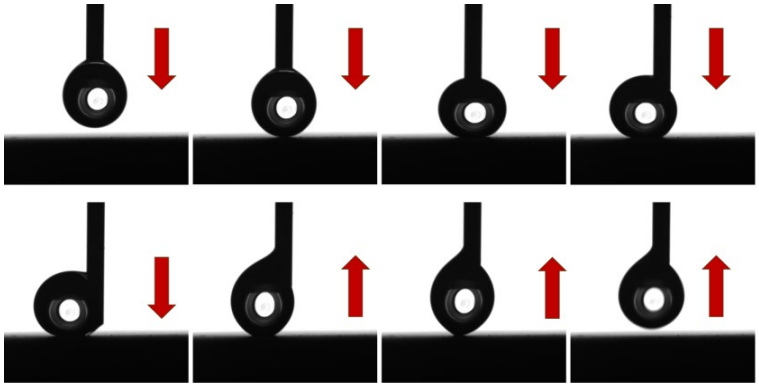

Fig. 10. Contact process of 5 μL water droplets and the surface of superhydrophobic NAB

4. Conclusion

In summary, the novel labyrinth microstructure interconnected by micron and submicron acicular structures was successfully obtained via etching NAB in 9 wt% $FeCl_3 \cdot 6H_2O$ solution at room temperature for 40 min. Once modified with FAS-17, the labyrinth microstructure has robust superhydrophobicity with a static water CA of 163.4° and a RA of ≤ 10 °. Besides, the low-adhesion SHS presents excellent inhibition effect to the NAB corrosion and stability in 3.5 wt% NaCl solution with different pH values. The air trapped in the low-adhesion SHS is the essential contributor of the excellent anticorrosion property for its insulation, the particular labyrinth microstructure composed of micron and submicron acicular structures acts as a “frame” to trap air as well as a coating with inhibition effect. This method is facile to operate, and it is expected to accelerate the use of the low-adhesion SHS in the anticorrosion of engineering copper alloy.

References

[1] S. Q. Zeng, J. J. Tian, S. B. Hu, M. Xiao, B. Peng, Transactions of Nonferrous Metals Society of China, 33, 2090(2023); https://doi.org/10.1016/S1003-6326(23)66246-6

[2] R. C. Barik, J. A. Wharton, R. J. K. Wood, K. S. Tan, K. R. Stokes, Wear, 259, 230(2005); https://doi.org/10.1016/j.wear.2005.02.033

[3] F. Wang, R. R. Ma, Y. Q. Tian, Industrial Crops and Products, 184, 115010(2022);

https://doi.org/10.1016/j.indcrop.2022.115010

[4] R. R. Hashjin, Z. Ranjbar, H. Yari, G. Momen, Surfaces and Interfaces, 33, 102282(2022); https://doi.org/10.1016/j.surfin.2022.102282

[5] H. Jie, Q. J. Xu, L. Wei, Y. L. Min, Corrosion Science, 102, 251(2016); https://doi.org/10.1016/j.corsci.2015.10.013

[6] H. Y. Wang, Y. X. Zhu, Z. Y. Hu, X. G. Zhang, S. Q. Wu, R. Wang, Y. J. Zhu, Chemical Engineering Journal, 303, 37(2016); https://doi.org/10.1016/j.cej.2016.05.133

[7] W. Qian, Y. Q. Hua, R. F. Chen, P. Xu, J. Yang, Materials Letters, 268, 127570(2020); https://doi.org/10.1016/j.matlet.2020.127570

[8] C. Kang, H. F. Lu, S. J. Yuan, D. Y. Hong, K. P. Yan, B. Liang, Chemical Engineering Journal, 203, 1(2012); https://doi.org/10.1016/j.cej.2012.06.128

[9] C. X. Wang, X. Xiong, L. Yang, Y. Hong, S. H. She, H. Zhang, H. B. Liu, V. Ji, M. N. Li, Corrosion Science, 211, 110908(2023); https://doi.org/10.1016/j.corsci.2022.110908

[10] S. Öztürk, S. E. Sünbül, A. Metoğlu, K. İçin, Tribology International, 151, 106519(2020); https://doi.org/10.1016/j.triboint.2020.106519

[11] W. Y. Wang, W. J. Zhang, Y. F. Liu, J. Zou, X. J. Mi, D. D. Li, K. Y. Li, G. J. Huang, Corrosion Science, 215, 111049 (2023); https://doi.org/10.1016/j.corsci.2023.111049

[12] Y. T. Lv, Y. Ding, H. Z. Cui, G. H. Liu, B. H. Wang, L. M. Cao, L. Li, Z. B. Qin, W. J. Lu, Materials Characterization, 164, 110351(2020); https://doi.org/10.1016/j.matchar.2020.110351

[13] T. Murray, S. Thomas, Y. X. Wu, W. Neil, C. Hutchinson, Additive Manufacturing, 33, 101122(2020); https://doi.org/10.1016/j.addma.2020.101122

[14] S. M. Orzolek, J. K. Semple, C. R. Fisher, Additive Manufacturing, 56, 102859(2022); https://doi.org/10.1016/j.addma.2022.102859

[15] J. H. Han, E. H. Liu, Y. Q. Zhou, S. Zhao, H. Y. Yan, C. X. Hu, J. H. Kang, Q. Han, Y. Y. Su, Materials Today Communications, 34, 105085(2023); https://doi.org/10.1016/j.mtcomm.2022.105085

[16] T. H. Naing, S. Janudom, N. Mahathaninwong, W. Limbut, S. Karrila, Materials Today Communications, 35, 106241(2023); https://doi.org/10.1016/j.mtcomm.2023.106241

[17] W. Liu, Q. J. Xu, J. Han, X. H. Chen, Y. L. Min, Corrosion Science, 110, 105(2016); https://doi.org/10.1016/j.corsci.2016.04.015

[18] G. Whyman, E. Bormashenko, Langmuir, 27, 8171(2011); https://doi.org/10.1021/la2011869

[19] L. Zhao, Q. Liu, R. Gao, J. Wang, W. L. Yang, L. H. Liu, Corrosion Science, 80, 177(2014); https://doi.org/10.1016/j.corsci.2013.11.026

[20] Y. Feng, W. -K. Teo, K. -S. Siow, K. -l. Tan, A. -K. Hsieh, Corrosion Science, 38, 369(1996); https://doi.org/10.1016/0010-938X(96)00110-2

[21] M. Diafi, A. Aidi, B. Benhaoua, Digest Journal Of Nanomaterials And Biostructures, 15, 621(2020); https://doi.org/10.15251/DJNB.2020.153.621

[22] S. Gao, X.D. Li, M. Zhang, Digest Journal Of Nanomaterials And Biostructures, 16, 1565(2021); https://doi.org/10.15251/DJNB.2021.164.1565

[23] Q. Gao, J. Li, R. Ma, Y. Fan, A. Du, M. Yang, X. Zhao, Y. Bian, Materials Today Communications, 37, 107032(2023); https://doi.org/10.1016/j.mtcomm.2023.107032

[24] K. Ellinas, A. Tserepi, E. Gogolides, Advances in Colloid and Interface Science, 250, 132

(2017); https://doi.org/10.1016/j.cis.2017.09.003

[25] B. B. Zhang, Q. J. Zhu, Y. T. Li, B. R. Hou, Chemical Engineering Journal, 352, 625(2018); https://doi.org/10.1016/j.cej.2018.07.074

[26] L. Liu, W. K. Liu, R. F. Chen, X. Li, X. J. Xie, Chemical Engineering Journal, 281, 804(2015); https://doi.org/10.1016/j.cej.2015.07.028